Green Chemistry

PAPER

View Article Online
View Journal | View Issue

Check for updates

Cite this: *Green Chem.*, 2025, **27**, 9706

Engineering low-carbon fiber cement with biochar: understanding its physicochemical properties and their impact on the composite performance and carbon footprint†

Sreenath Raghunath, [a,b] Mahfuzul Hoque, [a,b] Akash Madhav Gondaliya,[a,b] Adel Jalaee,[a,b] Behzad Zakani,[a,b] Fernanda Brito dos Santos,[a,b] Qingshi Tu[b,c] and E. Johan Foster *[a,b]

To address the United Nations sustainable development goals in combating climate change, this study explores the use of biochar as a supplementary cementitious materials (SCMs) for developing low-carbon, non-structural building materials such as fiber cement. Since understanding the role of biochar in influencing the physicochemical characteristics of fiber cement is central to material development, herein, we have performed in-depth rheo-mechanical characterization. The static yield stress (rheological) of the fiber cement slurry increased by 98% with biochar content of 10 wt%, whereas the dynamic yield stress did not change substantially. The thixotropic properties was also improved with biochar content (*vs.* control), indicating more pronounced time dependent shear thinning behaviour and structural rebuilding at rest. The mechanical properties of the cured composite increased by 40% with biochar content of 8 wt%. Furthermore, a combination of solid-state spectroscopic studies and microstructural visualization provided insights about the contributing factors to strength development. Notably, biochar porosity and surface chemical functionality played a vital role in improving the OPC hydration. Finally, upon cradle to gate life cycle analysis (LCA) and cost to performance analysis (C/P), we learned that 8 wt% biochar substitution achieved the best C/P balance while reducing global warming potential (GWP) by 18%.

Received 20th March 2025,
Accepted 1st July 2025

DOI: 10.1039/d5gc01405k

rsc.li/greenchem

Open Access Article. Published on 04 July 2025. Downloaded on 4/7/2026 8:36:45 PM.
This article is licensed under a Creative Commons Attribution-NonCommercial 3.0 Unported Licence.

Green foundation

1. This work integrates inorganic cement chemistry with organic biochar chemistry to develop low-carbon fiber cement composites. It aligns with green chemistry principles by utilizing waste-derived carbon materials to reduce emissions and promote sustainable construction.
2. Biochar enhanced fiber cement aligns with green chemistry principles (1, 4, 6, 7 & 10). The presence of surface functional groups in biochar improves hydration and mechanical performance without the need for employing additional synthetic additives – principle 4 (designing safer chemicals). It aligns with principles 7 &10 (use of renewable feedstocks & design for degradation) by replacing conventional SCMs with processed waste biomass capable of storing fixed carbon. A cradle-to-gate LCA shows an 18.1% GWP reduction, aligning with principles 1 & 6 (prevention & design for energy efficiency).
3. Enhancing biochar's pozzolanic reactivity, CO_2 curing, and using low-carbon cement blends (*e.g.*, metakaolin and fly ash) can improve sustainability.

Introduction

Low-carbon building materials are essential in lowering the carbon footprint of construction industries, which predominantly use ordinary Portland cement (OPC). Fiber cement (FC) manufacturing utilizes natural fiber, *e.g.*, wood derived pulp fiber mixed with OPC and various silica-based fillers, and a plasticizer prior to air or autoclave curing. Thus, in recent research on high-density FC, silica-based fillers and petrochemical-derived plasticizers have been replaced with cellulose nanocrystals (CNCs)[1] and micro-cellulosic additives.[2] However,

[a]*Department of Chemical and Biological Engineering, The University of British Columbia, 2385 East Mall, Vancouver, BC V6T 1Z4, Canada*
[b]*Bioproducts Institute, 2385 East Mall, Vancouver, BC V6T 1Z4, Canada. E-mail: johan.foster@ubc.ca*
[c]*Department of Wood Science, University of British Columbia, 2424 Main Mall, Vancouver, BC V6T 1Z4, Canada. E-mail: qingshi.tu@ubc.ca*
† Electronic supplementary information (ESI) available. See DOI: https://doi.org/10.1039/d5gc01405k

This journal is © The Royal Society of Chemistry 2025

Open Access Article. Published on 04 July 2025. Downloaded on 4/7/2026 8:36:45 PM.
This article is licensed under a Creative Commons Attribution-NonCommercial 3.0 Unported Licence.

these cellulosic additives have limited carbon sequestration potential owing to their lower filler content (in wt%). While new cement manufacturing or matrix modification methods are being developed,[3–5] OPC still dominates global cement production. Substituting OPC with a low carbon biobased/biogenic material is an excellent material design strategy to reduce the environmental impact of conventional OPC, which contributes to ~8% of global CO_2 emissions under the United Nations sustainability development goal (especially SDG 11).[6]

As a biogenic material, biochar has garnered interest for various applications, with one such example being the development of "eco-friendly" structural building materials.[7] Biochar is a carbon-rich solid waste, produced during the biomass-bioenergy generation process *via* controlled pyrolysis (300–700 °C, with little or no oxygen).[8] Its amorphous carbon structure renders a low ratio of H/C (hydrogen to carbon) and O/C (oxygen to carbon), which is also observed for soot and carbon black.[9] Overall, the chemical composition and morphology of biomass depend on the biomass type and pyrolysis process parameters.[10] Nonetheless, as a carbon sequestering material, it offers a pathway to remove CO_2 permanently from the atmosphere as it stores carbon in a stable chemical form. In other words, buildings made with biochar have become a permanent sink for carbon. For instance, it is estimated that the use of biochar technology can eliminate up to about 1.7–3.7 $PgCO_2eq.$ of CO_2 [11] from the atmosphere, which iterates the immense possibility of utilizing biochar in various applications to mitigate climate change.

In the case of FC, materials chemistry of biochar (particle size, chemical composition and pH) can play a crucial role beyond green chemistry, like improving the hydration kinetics and modification of rheo-mechanical properties. To date, as supplementary cementitious materials (SCMs), majority of the biochar use cases have focused on cement mortar and ultra-high-performance concrete. Organic residues in biomass are converted into amorphous carbon (low H/C and O/C); such a chemical composition are known to retard the cement hydration reaction. Also, particle size and morphology of biochar are intrisically heterogeneous. In a recent report from Roychand *et al.*, it was found that biochar from spent coffee grounds improved the compatibility between the cement matrix and the biogenic SCMs.[12] Dixit *et al.*[13] explored the particle size effect of biochar and looked at its dual roles, as an internal curing agent and SCMs. Note that manually ground biochar was first presoaked in water prior to composite fabrication. Notably, at 5 wt% of finer (<250 μm) biochar particles, cement hydration was accelerated, and higher heat release was observed as opposed to coarser (>250 μm) ones. It was speculated that finer biochar particles have the ability to adhere to the positively charged clinker phases owing to the higher surface area and create more nucleation points, thereby accelerating hydration. Furthermore, Gupta *et al.*[14] reported that the particle size of biochar plays a pivotal role in tuning the rheology (*i.e.*, static yield stress) of cement paste by using a ball milling (BM) method.[14] Interestingly, coarser biochar particles (avg particle size ≈ 45–50 μm & 2 vol% addition) increased the static yield stress 1.8–2.7 times, compared with BM (avg particle size: 10–18 μm).

Furthermore, the effect of biochar content on biochar mechancial properties were investigated to by varying the biomass source. In two separate studies by Choi *et al.*[15] and Gupta *et al.*,[16] the incorporation of biochar at 5 wt% (biomass source: switchgrass) and 2 vol% (biomass source: locally collected saw dust) dosages led to an increase in compressive strength by 10% (28 days curing) and 40% (7 days curing), respectively. However, for non-structural application, Restuccia and Ferro[17] reported that at 0.8 wt%, the flexural strength of the cement mortar increased by 30% (28 days curing).[17] Similar results were obtained by Khushnood *et al.*;[18] at 0.2 and 0.080 wt%, the flexural strength after 28 days of curing improved by 83% and 80%, respectively. Durability of composite is also an important peformance metric alongside mechanical properties. Sirico *et al.*[19] evaluated the effect of wood waste derived biochar on the wet/dry strength of concrete – 5 wt% addition contributed to 30% increase in compressive strength. Overall, the effect of biochar size and content on cement hydration and composite mechanical properties are evident in these previous studies, but the exact mechanism is still unknown. Particle size reduction provides benefits, but appropriate size characterization techniques are lacking since the biochar particle shape is heterogeneous. Regardless of the biomass source, mechanical strength is not compromised by the addition of biochar, but none of the reports convey its role in fiber reinforcement.

In this research, we have utilized biochar as a cement supplement to engineer low-carbon fiber cement. A planetary ball milling method is used to homogenize biochar particle size. Physico-chemical characterization of biochar is complemented with rheo-mechanical-microstructure characterization of the composite (pre and post curing). A solid-state particle size analysis technique (denoted as dynamic image analysis, DIA) was utilized to depict the effect of mechanochemistry on biochar and how that impact composite performance. We believe this study will advance new avenues in "eco-friendly" building material development for a low carbon society, a key driver to reach our sustainable development goals by 2050.

Materials, fabrication and characterization methods

Raw materials. The cement (Type 1, ordinary Portland cement) used for this research was procured from Lafarge, Canada, and was used as received. The Northern bleached softwood kraft pulp (NBSK) employed for this research was procured from Canfor (Prince George Paper Mills), Canada. Biochar was procured from BC Biocarbon, Canada (brand name: "Black Bear Biochar" (<2 mm) derived from wood forest residues). Unless otherwise specified, reverse osmosis (RO) water was used for this research. The pulp fibers and biochar were subjected to preprocessing steps, which are mentioned in the fabrication section below. The composition and physical properties of the raw materials employed for this research are described in Tables S1–S7.†

Open Access Article. Published on 04 July 2025. Downloaded on 4/7/2026 8:36:45 PM. This article is licensed under a Creative Commons Attribution-NonCommercial 3.0 Unported Licence.

Fabrication of the fiber cement. The first step in FC manufacturing involved refining the pulp fibers to induce fibrillation, which is critical for enhanced fiber–fiber bonding and to promote efficient load transfer. For this, 24 grams of oven dried NBSK were first soaked in 2 liters of deionised (DI) water (overnight, approximately 12 hours). The soaked pulp was then subjected to disintegration, followed by vacuum filtration to remove excess water. The filtered fibers at 10% consistency were then fed into a NORAM PFI mill (model: PPCT1008) and refined for 4500 revolutions of the PFI mill (see Tables S3 and S4† for refined fiber properties). The refining protocol mentioned was adapted from prior literature studies.[20] Note that for all samples prepared for this study, the refined NBSK fiber content was fixed at 8 wt%, serving as the baseline to systematically evaluate the influence of varying biochar content on FC performance.

Biochar, which is inherently heterogeneous (particle size, chemical composition, *etc*.), was subjected to a mechano-chemical process. A planetary ball milling device (PM 400, Retsch, Germany) was used along with stainless-steel balls (bearing size: 6.35 mm in diameter, ball/powder ratio: 20 : 1) for 45 minutes. The ball milled (BM) biochar (labeled as BC_BM, see Table 1 for sample composition and Tables S5–S7† for biochar physio-chemical properties) was premixed with cement; the NBSK fiber was then added to the mixing bowl at a constant water/binder ratio of 0.5. As a benchtop small-scale mixer, a kitchen-grade Techwood 6QT (power output: 800 W) was used, operating at 600 rpm for 6 minutes. The mixing process was carried out at intermittent intervals (*i.e.*, 2 minutes). It is an important step since scraping the cement pastes that adhere to the side and bottom of the mixing bowl, and these breaks ensure the mixture is as homogeneous as possible (see Fig. S1† for detailed FC fabrication steps).

After the mixing process, the resulting FC slurry was transferred into a metallic mold of dimension 30 × 20 × 0.8 cm and placed on a vibrating microplate shaker (from Thermo Fisher, Canada) for 15 min at 300 rpm for compaction. After compaction, the FC samples were air-cured for 28 days (demolded after 7 days and the samples were placed in a plastic bag). All the sample preparations were carried out at a temperature of 23 ± 2 °C and at a relative humidity of 50 ± 4 °C. For rheological characterization, slurry state samples were utilized, and for mechanical and microstructural characterization, hardened state samples were utilized. The sample composition is illustrated in Table 1.

From Table 1, it may be noted that the total binder mass (*i.e.* cement + biochar) was held constant for all samples prepared for this study. The individual proportions of cement and biochar were systematically varied for each sample, but the total binder mass remained constant (*i.e.*, when the cement content was decreased, the biochar content was increased to match the fixed binder mass). The weight percent of all other FC constituents such as NBSK fibers, water, *etc*. was taken relative to the fixed binder mass. While we acknowledge that replacing cement in proportions with a lower density material such as biochar can affect the solid volume fraction, the use of fixed binder mass was done to maintain a fixed water/binder ratio. This isolates the specific effect of biochar on the rheo-mechanical performance of FC. Such experimental design is commonly adopted in cement/composite research and ensures consistency and direct comparison of results.[1,2,22]

Solid-state biochar and fiber cement characterization

Particle size analysis. To understand the effect of ball milling on the particle size of biochar, a dynamic image analysis (DIA) analyser from Sympatec, GMBH, Germany (model: QICPIC + RODOS) was used. The biochar samples (both unmilled and milled, approximately 3 g) were fed (at a constant feeding rate of 20%) into the vibrating dispenser of the DIA device. The open jet aerosol disperses particles that pass through an analysis chamber housed with a high-definition camera that records and computes the shape and size characteristics of individual particles. During the experiment, a constant sample feeding rate of 20% was used with a 2 mm gap width. Particles were dispersed under 1 bar primary pressure and a vacuum pressure of 14 mbar to ensure clean aerosolization and minimal agglomeration. A frame rate of 175 Hz and an optical concentration range of $C_{opt,start} \geq 0.02\%$ to $C_{opt,end} \leq 0.02\%$ were maintained to allow for accurate measurement of individual particles. The EQPC (equal area projection of

Table 1 List of fabricated fiber cement tested to evaluate the rheo-mechanical properties. The sample nomenclature follows the format BC_BM-*x*, which corresponds to FC containing ball milled biochar in varied proportions (*i.e.*, '*x*' wt%). All samples contain 8 wt% of refined NBSK fibers in them and only the binder content (*i.e.*, cement/biochar) varied proportionally to the FC constituents is tabulated in vol% and is used throughout the manuscript where applicable. The range of biochar loading used for this study was chosen based on the findings from past literature studies[21]

	Binder							
	Cement		Biochar		NBSK fiber		Water	
Sample ID	wt%	vol%	wt%	vol%	wt%	vol%	W/B	vol%
BC_BM-0 (control)	100 (420 g)	53.38	0 (0 g)	0	8 (33.6 g)	8.18	0.5	38.44
BC_BM-2	98 (411.6 g)	49.44	2 (8.4 g)	6.51	8 (33.6 g)	7.73	0.5	36.32
BC_BM-4	96 (403.2 g)	45.90	4 (16.8 g)	12.35	8 (33.6 g)	7.32	0.5	34.43
BC_BM-6	94 (394.8 g)	42.71	6 (25.2 g)	17.61	8 (33.6 g)	6.96	0.5	32.72
BC_BM-8	92 (386.4 g)	39.83	8 (33.6 g)	22.37	8 (33.6 g)	6.63	0.5	31.17
BC_BM-10	90 (378 g)	37.21	10 (42 g)	26.70	8 (33.6 g)	6.33	0.5	29.77

 This journal is © The Royal Society of Chemistry 2025

Open Access Article. Published on 04 July 2025. Downloaded on 4/7/2026 8:36:45 PM. This article is licensed under a Creative Commons Attribution-NonCommercial 3.0 Unported Licence.

circle) method was used by the device to calculate the particle size of the biochar particles.[23]

Compared to the conventional laser diffraction system employed for analysing the particle size, the QICPIC + RODOS configuration provides a unique advantage of capturing real-time 2D images of individual particles, allowing for simultaneous measurement of both particle shape and size. While laser diffraction based particle analysers rely on light scattering patterns assuming a spherical shape geometry to generate particle size distribution, image-based analysis does not rely on any assumptions but rather uses fractal dimensions (based on the captured 2D image of the particle) to compute particle shape and size effectively.[24] This makes QICPIC + RODOS particularly useful for analysing irregularly shaped particles such as biochar, where particle morphology significantly dictates the resulting composite material performance.[24] In addition to this, the high speed imaging using the QICPIC system enables the detection of agglomerates and shape outliers, which laser diffraction may not be able to distinguish, and this helps us to understand the particle size distribution more effectively.[24]

Raman spectroscopy. Raman spectrographs of the biochar samples (before and after ball milling) were recorded using an Invia Reflex confocal Raman microscope (Renishaw, UK). Two different laser excitation wavelengths were employed (532 nm & 785 nm) to facilitate the surface and bulk level characterization of both the biochar samples. The Raman spectrum was recorded in the range from 1000 to 3000 cm^{-1}. Measurements were made at 5 different spots on the sample and the respective spectra were averaged.

X-ray photoelectron spectroscopy (XPS). To characterize the surface functional groups and state of the elemental composition of biochar, an X-ray photoelectron spectrometer (Kratos AXIS Supra, UK) with a monochromatic Al Kα source (15 mA, 15 kV) was used. The work function of the instrument was calibrated to provide a binding energy (BE) of 83.96 eV for the line of metallic gold ($4f_{7/2}$), whereas the spectrometer dispersion was adjusted to deliver a BE of 932.62 eV for the line of metallic copper (Cu $2P_{3/2}$). Note that all the specimens were subjected to the Kratos charge neutralizer system to compensate for charge buildup, which is synonymous in the case of non-conducting materials. An analysis area of 300 × 700 μm and a pass energy of 160 eV were used for the surface scan. For the high-resolution scan, 300 × 700 μm and a pass energy of 2 eV were utilized. The aliphatic carbon 1s signal, set to 284.8 eV, was used for the charge correction of all the spectra. Spectrum analyses were carried out using CasaXPS software (Version 2.3.26), and the graphs were plotted using OriginPro 2023 software.

Rheological characterization. The rheological characterization of the FC slurry was performed using a rheometer from NETZSCH Malvern, UK (model: Kinexus ultra+). The measuring system was a 4-blade vane-in-cup. To impart consistency and to negate the effect/interference of cement hydration reaction with the rheological results, all the tests were carried out at an early time period of 8 ± 1 min after the mixing process. Approximately 33 mL of the mixed FC slurry was utilized for this analysis.

The FC slurry (supplemented with various proportions of biochar) was fed into the sample holder and was subjected to two different analyses: (a) steady state viscometry (to understand the trends in viscosity with the shear rate) and (b) strain amplitude sweep (to compute static and dynamic yield stress). Steady-state viscometry was carried out within a high-to-low shear rate regime (1000–0.01 S^{-1}) at a temperature of 25 ± 1 °C.

To calculate the static yield stress, a strain amplitude sweep was performed, ranging from 0.01% to 1000%. For the dynamic yield stress, strain amplitude measurements were conducted in reverse order, from 1000% to 0.01%. Both tests were carried out on freshly prepared samples. The yield stress for both static and dynamic measurements was defined as the shear stress at the crossover point between the elastic (G') and viscous (G'') moduli.

Mechanical characterization. Mechanical characterization (three-point bending test) was done using a universal testing machine (UTM) from INSTRON, USA (model: 5969) to ascertain the flexural strength of the biochar-supplemented FC composite. From the cast samples, a rectangular block of size 19.5 × 4.5 × 0.8 cm was cut to perform the test. A crosshead speed of 10 mm min^{-1} was chosen for the test. All the tests were carried out on the 28th day of curing and the test itself was carried out as per ASTM C1185 standard requirements.[25]

The flexural stress σ_f and strain ε_f during a three-point bending test can be calculated using the following formulas:

$$\sigma_f = \frac{3PL}{2bd^2} \quad (1)$$

$$\varepsilon_f = \frac{6Dd}{L^2} \quad (2)$$

where σ_f – flexural stress in a material under the three point bending test, P – applied load (N), L – span length between supports (mm), b – specimen width (mm), d – specimen thickness (mm), ε_f – flexural strain in a material under the three point bending test and D – mid-span deflection (mm) obtained from displacement data. For determining the modulus of rupture (MOR), the value of P used in eqn (1) corresponds to the maximum load recorded during the test.[25]

At this juncture, it is important to emphasize that three point bending tests were conducted on reduced scale specimens in accordance with ASTM C1185. Due to this, the mechanical size effect – such as that described by Bazant's size effect law (which indicates how the nominal strength of a structure changes with size, particularly in quasi-brittle materials like concrete)[26,27] – and related scaling models[28] are known to influence the apparent strength of fiber reinforced cement composites; its impact may however be limited in thin FC samples (8 mm thickness), particularly employed for non-structural applications (such as in this case). Nonetheless, this factor needs to be considered when interpreting flexural test results, particularly when extrapolating to full scale panel behaviour or when translating our current use case scenario to more structural applications (such as for concrete applications).

Open Access Article. Published on 04 July 2025. Downloaded on 4/7/2026 8:36:45 PM. This article is licensed under a Creative Commons Attribution-NonCommercial 3.0 Unported Licence.

Porous structure analysis. The surface area, pore volume, and pore size distribution of the biochar samples (BC_RAW & BC_BM) were measured using a BELSORP-mini II, high precision surface area and porosity analyzer from Microtrac, USA using the N_2 absorbate at −196 °C. All biochar samples were degassed at 110 °C under vacuum for 16 hours before conducting the test.

Powder X-ray diffraction (PXRD). To analyze the phases present in the biochar as well as to identify the phases of cement hydration products with the addition of biochar, powder X-ray diffraction (PXRD) was performed using a Bruker D-8 Advance X-ray diffractometer with a Bragg–Brentano configuration. The X-ray radiation (Cu $K\alpha_1$ & $K\alpha_2$, λ_0 = 1.54056 & 1.54439 nm) with a generator specification of 40 kV, 40 mA was used, and a nickel filter was utilized to cut down the $K\alpha_2$ radiation. The specification of the detector slit comprises a 0.6 mm divergent slit, an 8 mm anti-scatter slit, and a 2.5° soller slit, and a LYNXEYE silicon strip detector was employed. The diffraction pattern was recorded from 5–90°, and a Bragg angle (2θ) with a step size of 0.03° was used to record the diffractograms.

For probing the phase ID of the biochar samples, the sample as received from the vendor (in powdered form) was packed into the sample holder of the XRD machine and analyzed. For probing the phase ID of cement hydration products with the addition of biochar, the 28 day cured FC sample containing biochar was subjected to mild mechanical pulverization using a 700 W mixer from Black + Decker, USA. The powdered sample was then sieved through a USA standard testing sieve (mesh size of MS 100, ASTM E-11); this was done to maximize the probability of probing the hydration products. The sieved samples were packed in the XRD sample holder and analyzed for their hydration products.

Electron microscopy. To understand the structural changes in biochar before and after ball milling (BM) and to probe the fiber–cement interface containing BC, an SEM from Field Emission Instrument (FEI) company, USA (model: Helios Nano Lab 650) was utilized. The BC samples (before and after ball milling) were coated with iridium (since the samples were non-conductive) using a sputter coater (model: LEICA EM MED020, Germany) and analyzed for their microstructure.[29] To probe the FC interface containing biochar, sample preparation involves carrying out the same steps as mentioned in the above section for phase ID of cement hydration products. The pulverized and sieved FC samples were coated with iridium, as mentioned above, and analyzed for their microstructure.

Nuclear magnetic resonance (NMR) spectroscopy. To understand the effect of biochar supplementation on the hydration (formation of CSH phases, quantification and probing the structure and environment of silicate species) of cement composites, high resolution ^{29}Si SS (MAS) NMR analysis was carried out using an Avance III 400 NMR spectrometer (Bruker) at room temperature. The operation frequency was 400 MHz, and the spectra were recorded at single pulse excitation (with a pulse length of 3.8 μs and a delay of 180 s). The accumulation number for ^{29}Si was 384 scans. The 7 day cured cement samples (with and without biochar, subjected to mild mechanical pulverization, powdered and sieved) were packed in a Zirconium rotor (4 mm diameter) and spun at a frequency of 10 kHz. Note that for the NMR analysis, samples were prepared without NBSK fibers to effectively study the influence of BC_BM on OPC hydration. The chemical shifts (ppm) were referenced against tetrakis(trimethylsilyl)silane (−10.02 ppm and −135.7 ppm). The processing of the NMR data was carried out using Originpro 2023 software.

Life cycle assessment (LCA) and cost/performance (C/P) analysis. A life cycle assessment (LCA) study was carried out, following ISO 14040 & 14044 standards,[30] to determine the environmental impact of utilizing biochar as a biobased (in six different proportions) supplement to cement for FC manufacturing. Further details pertaining to this LCA study are provided in the ESI.†

The cost to performance analysis was carried out to evaluate the economic viability and scaling up potential of FC substituted with biochar. The performance metric of interest chosen was the specific strength of 28-day cured FC composites, obtained by dividing the mean MOR by the density of the FC sample. Cost here refers to the total fabrication cost of the FC sample – which was estimated by summing the cost of all processing steps (including raw material extraction and conversion), based on the system boundary use in LCA. Raw material costs were obtained from prior technoeconomic analysis and published market research (see Fig. S6 & Tables S13, S14† for detailed cost breakdown). The cost to performance ratio (CPR) was calculated by dividing the total FC fabrication cost by the specific strength of each sample with varied biochar loadings.

Results and discussion

Understanding of the biochar physicochemical properties

Size and morphology. Fig. 1 depicts the effect of ball milling on biochar particle size distribution. It is observed from Fig. 1 (a and b) that BC_RAW and BC_BM exhibited a multimodal particle size distribution peak, with a VMD of 324 μm & 125 μm, respectively; a 61% reduction of VMD for BC_BM (*cf.* Table 2). Interestingly, from the DIA images, ball milling contributed to the breakdown of the bigger/coarser biochar particles (~500–800 μm) into more finer particles. Such a reduction in particle size is vital when biochar is used in conjunction with cement as a matrix material to ensure good compatibility. Additionally, the process of ball milling can also influence the shape of the biochar particle – from Fig. S3,† it was observed that, larger biochar particles (in the range of 600–800 μm) tend to smoothen out and become more spherical upon ball milling, thereby further enhancing the compatibility between two matrix materials.

Now, to gain a deeper understanding of the morphology of biochar particles, we transitioned from the laser diffraction technique to electron microscopy. Fig. 1(c, d) and (g, h) depict the SEM images of biochar particles before and after ball milling. As seen from Fig. 1(c and d), biochar inherently con-

 This journal is © The Royal Society of Chemistry 2025

Open Access Article. Published on 04 July 2025. Downloaded on 4/7/2026 8:36:45 PM.
This article is licensed under a Creative Commons Attribution-NonCommercial 3.0 Unported Licence.

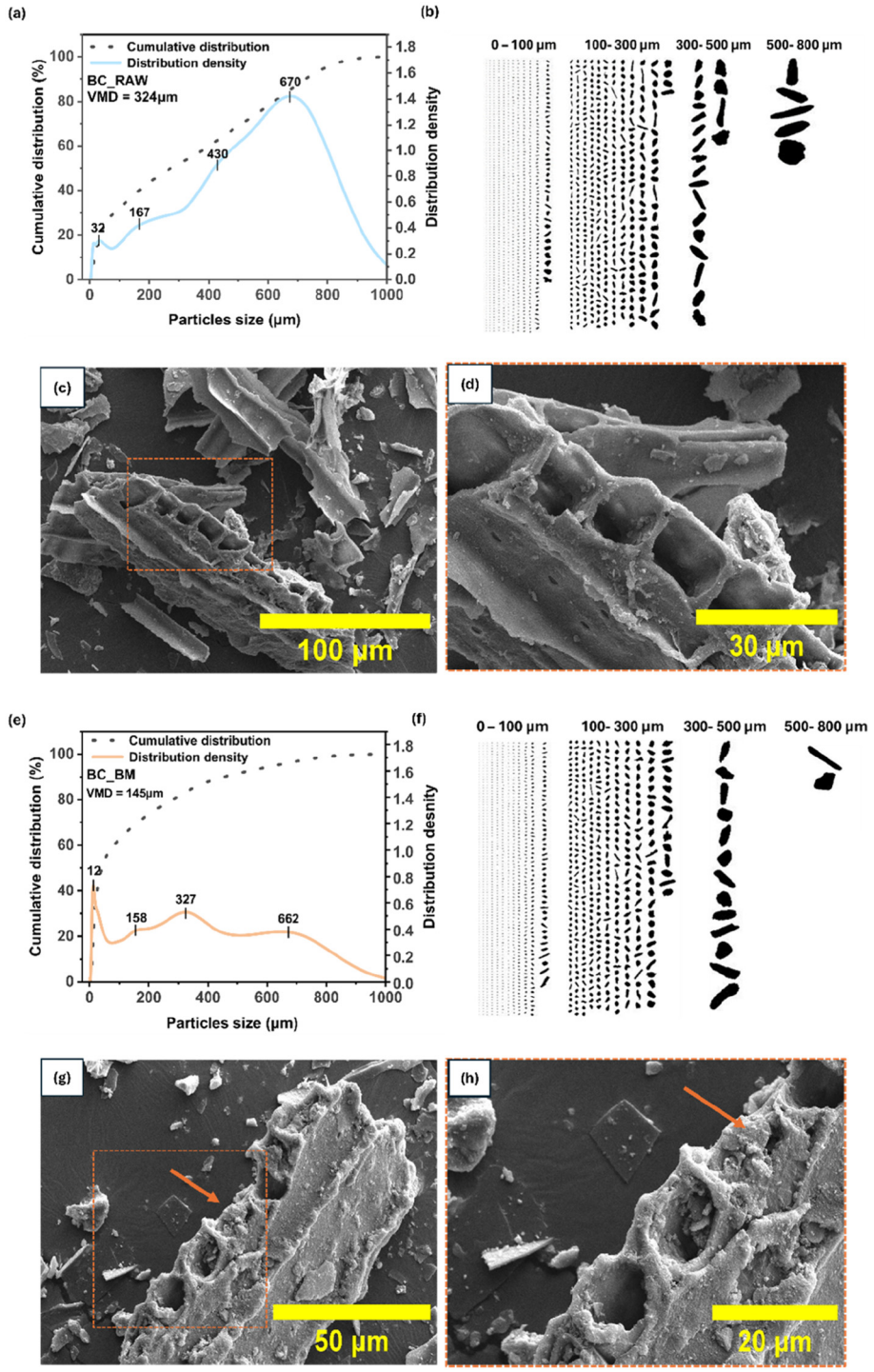

Fig. 1 Particle size and morphological characterization of biochar. Particle size distribution, DIA particle images and SEM micrographs of biochar (a–d) before (BC_RAW) and (e–h) after ball milling (BC_BM). In (g and h), the orange arrow indicates the collapsed pore structure.

Table 2 Effect of ball milling on the physical properties of biochar

Sample	Volume mean diameter, VMD (μm)	BET surface area, S_{BET} ($m^2\ g^{-1}$)	Pore volume, v_p ($cm^3\ g^{-1}$)
BC_RAW	324	429.4541	0.408102
BC_BM	125	391.1352	0.320178

sists of a porous honeycomb-like structure – when biomass undergoes pyrolysis, the organic components (such as cellulose, lignin, *etc.*) present in it decompose, whereas the cell structure (cell walls) often remains intact, giving rise to such structures.[31] Due to this, the resulting biochar particles tend to possess a high surface area and pore volume, which makes

Open Access Article. Published on 04 July 2025. Downloaded on 4/7/2026 8:36:45 PM.
This article is licensed under a Creative Commons Attribution-NonCommercial 3.0 Unported Licence.

them an ideal candidate as an additive/admixture for various applications.

Now, in addition to the reduction in particle size, the process of ball milling can have implications on the morphology of biochar structure. As evidenced from Fig. 1(e and f), some of the larger pores present in the biochar structure seemed to have collapsed upon ball milling (marked by the orange arrows, depicted in Fig. 1(g and h)). At this juncture, it is critical to note that high energy milling can indeed jeopardise the structural integrity of biochar samples if the milling parameters are not optimised. Therefore, upon optimization we chose 45 minutes (milling time), 20 : 1(ball to powder ratio) and 400 RPM as optimum milling parameters for this study, which is aligned with previous reports.[32]

Surface composition and carbon structure. Additionally, the process of ball milling can have ramifications with regard to the physical characteristics of biochar, such as surface area and porosity. Fig. 2(a and b) depicts the N_2 adsorption–desorption isotherm and BJH pore distribution plot of both the biochar samples. It could be observed from the N_2 adsorption–desorption isotherm that both biochar samples contain a combination of micro, meso, and macro-pores, and the BJH pore size distribution curve indicated a narrow monomodal distribution centered at the mesoporous region (pore width in the range of ~4.1 nm for both samples). Since the adsorption–desorption occurs predominantly in the high relative pressure domain, we can say that both our samples are considered to be mesoporous (2–50 nm) in nature (majority). Table 2 also describes the BET surface area and pore volume of both biochar samples, with the measured values in accordance with previously reported surface areas of high temperature pyrolyzed biochar.[33] Now, with ball-milling, (BC_BM), a slight reduction in both the BET surface area and the total pore volume by 9% and 21% respectively was observed, which could be attributed to the collapse of some of the biochar pore structures as evidenced in (Fig. 1g and h). It may be noted that the BET surface area seemed to reduce slightly with the ball milling process, contrary to our expectation that the surface area would increase upon ball milling. However, the contrary trend observed could be due to the reason that as the milling proceeds, the biochar particles may tend to smoothen out or form aggregates/agglomerates, which may potentially block the pores from being filled by the gas molecules during the analysis, resulting in a slightly reduced surface area measurement (this result in a way highlights the limitation of the BET technique itself in characterising the physical properties of materials with heterogeneous surface characteristics, especially when biobased materials are analysed – biobased

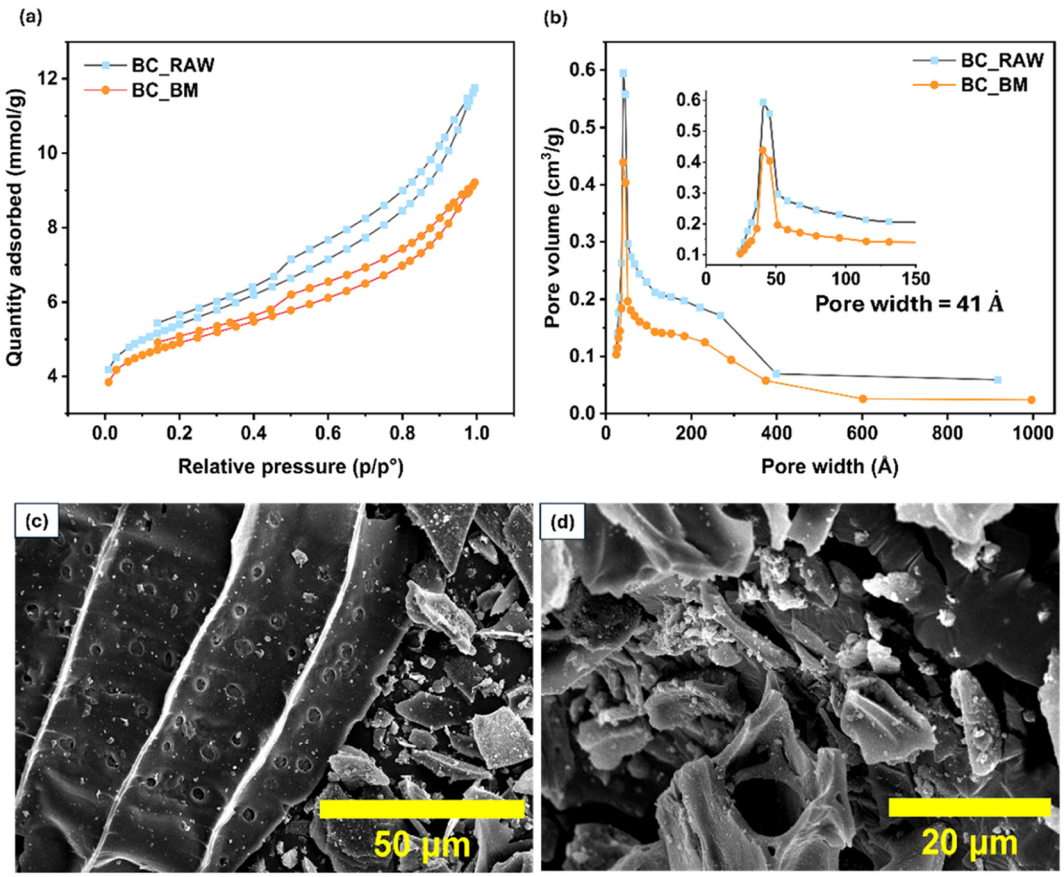

Fig. 2 Pore characterization and visualization of biochar. (a) N_2 adsorption–desorption isotherms and (b) BJH pore size distribution of biochar before (BC_RAW) and after ball milling (BC_BM). (c–d) Representative SEM micrographs of biochar after ball milling (BC_BM).

 This journal is © The Royal Society of Chemistry 2025

Open Access Article. Published on 04 July 2025. Downloaded on 4/7/2026 8:36:45 PM.
This article is licensed under a Creative Commons Attribution-NonCommercial 3.0 Unported Licence.

materials often contain volatile organic compounds/moisture trapped in the pores, which may result in incomplete degassing leading to underestimation of the surface area). Despite this, the majority of the pores (in the mesoporous region, *i.e.* between 2–50 nm) still remain intact (Fig. 2(c and d)), which suggests that the ball milling (for 45 minutes, in this case) process does not significantly destroy the structural integrity of the biochar samples.

Additionally, understanding the surface characteristics and carbon structure of the biochar is crucial to gauge the reactivity between alkaline cement matrix and biochar.[34]

Fig. 3(a) depicts XPS analysis of biochar surface, which is primarily composed of C (92.4 at%) and O (6.3 at%). Also, trace amounts of Al, Ca, Si and P (0.3, 0.4, 0.4, and 0.2 at%, respectively) were detected.[35]

From the deconvoluted XPS spectrum of carbon (C1s) as shown in Fig. 3(b), it can be inferred that surface chemistry of biochar is composed of unsaturated C=C bond, polar C–OH and C–O–C, O–C=O, C=O bonds, saturated C–C and C–H bonds[35,36] and π–π satellite[35–37] in relative proportions of 79.3%, 4.2%, 1.6%, 3.0%, 6.4% and 5.5%, respectively. The carbon-carbon bonds make up the amorphous and graphitic structure of the biochar, which is chemically stable under strong alkaline condition. However, the hydroxyl and carboxyl linkages could be reactive under alkaline cement matrix. Next, from the deconvoluted spectrum of O1s as shown in Fig. 3(c), it can be inferred that $O1s_1$ (532.07 eV) and $O1s_2$ (533.46 eV) with a relative proportion of 62.9% and 37.1%, respectively were prodominanlty part of carbonyl and ester groups, respectively.[35,38–40] Fig. 3(d) presents the high resolution spec-

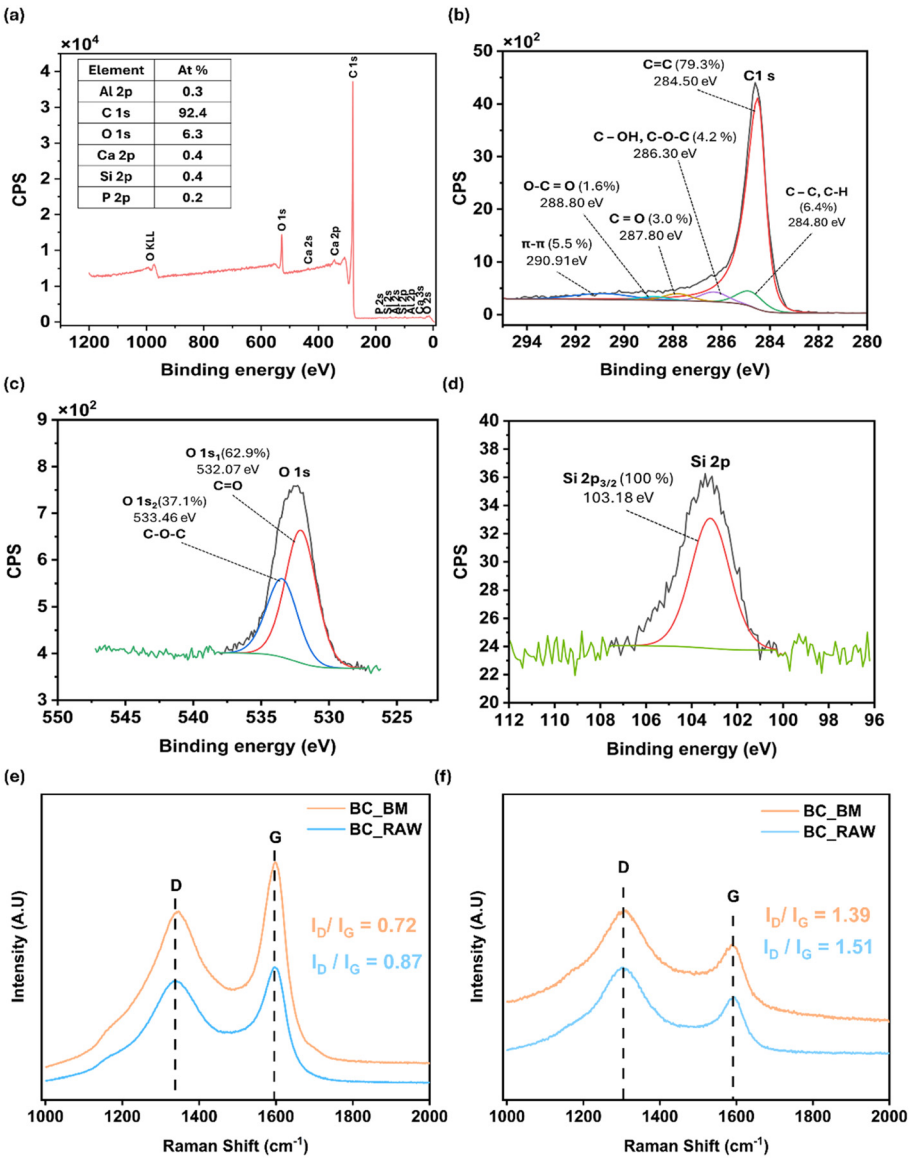

Fig. 3 Surface characterization of biochar. (a) Survey and (b–d) HR-XPS spectrum of raw biochar and (e–f) Raman spectra of raw and ball milled biochar under (e) 532 nm and (f) 785 nm laser excitation.

Open Access Article. Published on 04 July 2025. Downloaded on 4/7/2026 8:36:45 PM. This article is licensed under a Creative Commons Attribution-NonCommercial 3.0 Unported Licence.

trum of Si, and further in-detail deconvolution was not pursued as the proportions of silica present on the biochar surface is low.

Since biochar is a carbonaceous material, and ball milling can induce changes in its carbon structure, Raman spectroscopy was utilized to understand the effect of mechanochemistry.[41] In Fig. 3(e and f), two characteristics bands appear at around 1354 cm^{-1} ('D' band) and around 1596 cm^{-1} 'G' band, which are attributed to disorder/defect and sp^2 hybridised carbon atom associated to the crystalline graphitic layer, respectively.[42,43] The ratio of the intensities of 'D' and 'G' bands can provide a measure of the graphitization degree of the biochar samples. If the 'I_D/I_G' ratio is smaller, it indicates better graphitization or ordering of the stacked graphitic chains in biochar, and a higher ratio is indicative of a less ordered graphitic carbon structure.[41] Two different laser excitation wavelengths of 532 nm and 785 nm were used to probe the graphitization degree. The 532 nm laser is efficient at probing the surface level characteristics of the biochar sample, whereas employing a 785 nm laser will offer better penetration depth, thereby providing better insight into the bulk level characteristics of the biochar samples. Note that from Fig. 3(e and f), for two different excitation wavelengths, the 'I_D/I_G' ratio is observed to be slightly smaller in magnitude for ball milled samples compared with raw biochar samples (irrespective of laser excitation wavelength). This indicates possible mechanochemical effect by ball milling process on the carbon structure of biochar.

Though graphitization degree of biochar may not directly influence the rheo-mechanical performance of the fiber cement, higher graphitized biochar may potentially have a longer shelf life in the high alkaline environment of the cement matrix, which could prolong the overall performance (durability) of the composites.

Role of biochar in the rheological properties of the fiber–cement slurry

Static and dynamic yield stress analysis: implications on workability. Understanding the flow behaviour/characteristics of the FC slurry is of great importance as it dictates the feasibility of the FC fabrication process and its application. Cement pastes, in general exhibit a shear-thinning behaviour (see Fig. S3†) and possess yield stress. Due to their thixotropic nature, pastes typically exhibit two distinct yield points: static yield stress (τ_{static}) and dynamic yield stress ($\tau_{dynamic}$).[44] 'τ_{static}' defines the transition from solid to liquid-like state. Whereas '$\tau_{dynamic}$' represents the transition from a liquid to solid-like state.[45] In the context of the FC fabrication process, 'τ_{static}' provides a measure of flow initiation (crucial to mixing and consolidation of FC slurry) whereas '$\tau_{dynamic}$' becomes a critical parameter in maintaining the flow (useful in the case of pumping the mixed slurry). A variety of factors, such as the type and nature of additive/reinforcement/SCM employed, their concentration and surface chemical characteristics can influence the magnitude of yield stress of the FC slurry. Therefore, it is essential that we understand the effect of biochar and its influence on these critical rheological properties.

Moreover, cement hydration in presence of water is an exothermic reaction, leading to the formation of strength imparting hydration products such as calcium silicate hydrate (CSH). This is a continuous, time sensitive process where networked structures evolves in the fiber cement slurry. As such, it often complicates rheological measurements, particularly for long duration tests such as stress ramp or creep tests.[46,47] Thus, these methods, especially in systems undergoing active reactions often suffer from poor reproducibility and may negate subtle effects introduced by these additives.[47]

To tackle these limitations, we adopted oscillatory strain amplitude sweep tests, a relatively short-duration method that allows us to study the viscoelastic behaviour of the FC slurry, while ensuring minimal disruptions from ongoing hydration effects.[48] This method provides insight into early-age microstructural transitions and yields both static and dynamic yield stress and provides a direct measure of thixotropy of the FC slurry. The yield point is typically identified by the crossover of G' and G'' — the point at which the material transitions from elastic (solid-like) to a viscous (liquid-like) behavior.[46] The corresponding shear stress is then taken as the yield stress value.[46] This method provides a direct method for computing yield stress, unlike conventionally used viscometric models (such as *e.g.*, Bingham and Herschel–Bulkley), which are fitted to the steady state viscometry data (an indirect method) to compute yield stress viscoelastic materials.[49]

Another important factor that can influence the rheological measurement, especially while dealing with suspensions with high yield stress or fibrous content is the effect of wall slip and edge fracture.[50,51] To minimise these effects, we utilised vane in cup geometry – which is particularly useful for measuring the rheological properties of highly viscous samples compared to commonly employed parallel plate or concentric cylinder geometry. However, it may be noted that the complex stress distribution in the vane geometry is different from other geometries, therefore, absolute comparison of yield stress values is only possible if the test parameters and test geometry employed are similar. Given these critical constraints in terms of model assumptions, test methods, geometric effects, thixotropy and continuous cement hydration – our focus is to understand how biochar substitution affects the rheological properties of the FC slurry, within our well defined experimental framework.[51] Importantly, the results obtained by employing these well-defined protocols turned out to be consistent and reproducible, with varying biochar contents, offering valuable insights into the rheological characteristics of biochar substituted FC slurry.

As observed from Fig. 4(a), 'τ_{static}' of the FC slurry is highly dependent on the concentration of biochar. At a low content (0–2) wt%, 'τ_{static}' did not change significantly, indicating that the occurrence of yield stress is mostly concerned with the colloidal force and electrostatic interaction between the cement clinker phases as well as due to the structural build of cement hydration products (CSH network formation, see Fig. 4(a and b)),[52] note that for computing the 'τ_{static}' of the cement paste, the sample was kept at rest after the mixing process. However,

 This journal is © The Royal Society of Chemistry 2025

Open Access Article. Published on 04 July 2025. Downloaded on 4/7/2026 8:36:45 PM.
This article is licensed under a Creative Commons Attribution-NonCommercial 3.0 Unported Licence.

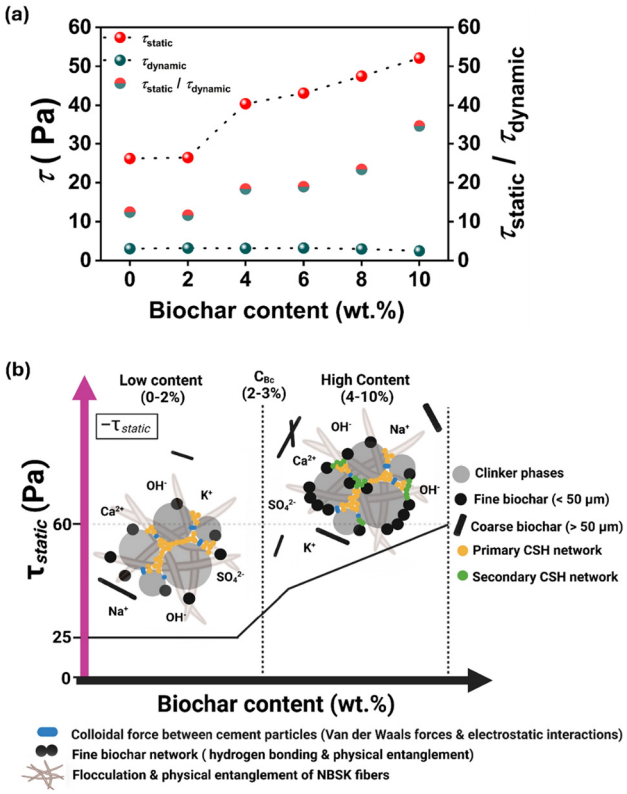

Fig. 4 Yield stress analysis of fiber cement slurry as a function of biochar content. (a) Variation of 'τ_{static}' & '$\tau_{dynamic}$' and '$\tau_{static}/\tau_{dynamic}$'. (b) Proposed mechanism of 'τ_{static}' evolution with biochar. Note that Ca^{2+}, Na^{+}, K^{+}, and OH^{-} depicted in the figure represents the ions present in the cement paste pore solution.

additional factors also contribute to 'τ_{static}' development in this domain (see Fig. 3(a and b)), such as the presence of coarser biochar (>50 µm) may behave as rigid inclusions within the FC slurry or may act as interlocking structures causing resistance to flow.[53] Additionally, the presence of NBSK fibers in the FC slurry (8 wt% in this case) would result in complex flocculation and physical entanglement (high aspect ratio fibers tend to entangle under shear) leading to agglomeration and increased resistance to flow (see Fig. 4(b)).[54,55] Therefore, a combination of these factors contributes to yield stress development (however, we believe that the role of biochar is considered minimal in this region). Now, as the biochar concentration rises from 2 to 4 wt%, the 'τ_{static}' increases rapidly (see Fig. 4(b)). We refer this concentration range as the critical biochar concentration 'C_{BC}', where an abrupt increase in 'τ_{static}' is observed (concentration range at which biochar begins to significantly influence the rheology of FC paste). This rapid increase in 'τ_{static}' could be attributed to the network formation of biochar within the FC slurry, causing a resistance to flow,[56] during the mixing process of FC slurry, some of the fine biochar particles can potentially buckle upon each other (due to possible hydrogen bonding) and form bridges connecting cement particles (electrostatic interactions), Fig. 4(b)). This could be attributed to the presence of surface functional groups in fine biochar (such as hydroxyl, carboxyl, and carbonyl groups) as evidenced through XPS (see Fig. 3(a and b)) and may promote the formation of hydrogen bonds with each other or with NBSK fibers promoting agglomeration and increasing resistance to the flow of the FC slurry.

Now, at high biochar concentrations (4–10 wt%), the 'τ_{static}' manifested a steady increase, reaching a maximum yield stress of 52.07 Pa at 10 wt% (98% increase *vs.* control, see Fig. 4(a)). Such an observation could be attributed to the following: (a) biochar particles forming networks that bridge cement particles, thereby increasing resistance to the flow of the cement slurry (*vide supra*) and (b) biochar particles adhering to cement particles during mixing, potentially acting as nucleation sites for OPC hydration products to develop[14] (referred to as secondary CSH, see Fig. 4(b)). Based on the data and characterization results, our hypothesis is that secondary CSH contribution is possibly minimal at low biochar dosages. Fine biochar particles (<50 µm) are more likely to contribute to nucleation effects, whereas coarser biochar (>50 µm) particles may act as rigid inclusions with limited reactivity. Therefore, the relative proportions of fine biochar in low biochar loading regime dictates the extent of secondary CSH formation. Additionally, the water absorption of NBSK fibers and biochar can tune the W/B ratio of the FC slurry, reducing the free water available in the FC and increasing the yield stress.[14] Also, biochar releases free water, maintaining moisture over time, which can promote hydration.[14] Thus, the aforementioned effects, possibly in-tandem contributes to the evolution of yield stress in the FC slurry marked by the steady rise at high biochar dosages. Additionally, it was observed from the Fig. 4(a) that '$\tau_{dynamic}$' remained largely independent of the biochar content. Perhaps, the formation of network structures (as discussed earlier) was delayed due to the continuous straining of the FC samples during oscillatory testing. As such, even at higher concentrations, the addition of biochar did not significantly affect the $\tau_{dynamic}$ of the cement slurry.

In this juncture, the '$\tau_{static}/\tau_{dynamic}$' ratio can be used as a direct measure of time dependent rheological properties such as thixotropy/rheopexy.[44,57] A ratio greater than unity suggests that the material is thixotropic in nature, meaning the slurry becomes less viscous under stress or strain and gradually recovers its viscosity once the stress is released. It is important to note that various factors can influence this behavior, and cement pastes often transition from thixotropic to rheopexic behavior over time. However, mixing and pumping of fiber cement slurry occur during the dormant phase of cement hydration, where the slurry/paste predominantly exhibits thixotropic behavior.[58] As shown in Fig. 4(a), the '$\tau_{static}/\tau_{dynamic}$' ratio for all biochar concentrations is well above 1, indicating that all FC samples exhibit thixotropic behaviour. Since '$\tau_{dynamic}$' remained unaffected by the biochar content, the '$\tau_{static}/\tau_{dynamic}$' ratio mirrored the trend observed in the '$\tau_{static}/\tau_{dynamic}$' evolution with varying biochar concentrations. Specifically, the ratio remained relatively constant at 0–2 wt% biochar and increased significantly from 2 to 10 wt%. Unique physico-chemical properties of biochar facilitate the formation

Open Access Article. Published on 04 July 2025. Downloaded on 4/7/2026 8:36:45 PM.
This article is licensed under a Creative Commons Attribution-NonCommercial 3.0 Unported Licence.

of a network structure within the slurry, leading to enhanced structural build-up. Consequently, as biochar content increases, the FC samples become increasingly thixotropic, which could be indicative of the improved restructuring and breakdown/rapid deflocculation[59] (upon shear/recovery at rest) of the fiber cement slurry constituents with time. Overall, thixotropic nature and its tunability could be advantageous for applications such as pumping and consolidation, where a material that maintains its structure under stress yet flows easily when needed.

Role of biochar on the mechanical properties of fiber cement

Flexural strength analysis and comparison with conventional carbon materials. Since FC is designed towards non-structural /load bearing applications, flexural strength, *vis a vis*, modulus of rupture (MOR) is characterized to evaluate mechanical performance. In this section, we demonstrated the effect of the biochar content on the flexural strength of the FC and the derived MOR values are compared against the traditional carbon materials.

Fig. 5(a) depicts the mechanical characteristics of FC with biochar pertaining to its bending behavior, a crucial criterion for non-structural building materials, like 8 mm thick building facades. The stress–strain curves in Fig. 5(a), reveals a relative rise in peak strength with increasing biochar content, accompanied by a reduction in post-peak deflection and post-crack toughness, suggesting loss/decline in ductile behaviour and energy absorption after the failure of the FC sample (*vs.* control). Such behaviours are common in FC composites and a similar trend was observed in our prior studies with the inclusion of cellulosic nano/micro-particles in FC.[1,2] Such a transition could be ascribed to the high packing density of biochar (ball milled) particles, as they render a void filling effect. Densification of the cement matrix makes the FC to become stiffer (brittle) compared with the control, albeit enhancing the ability of the composite to withstand higher mechanical load and delay the initiation of microcracks.[60,61]

From Fig. 5(a), it may also be noted that the control fiber cement exhibited improved strain hardening behaviour under flexural loading, characteristics of effective fiber bridging and crack resistance. It is important to note that despite the improvement of peak strength, the inclusion of even a low dosage of biochar (BC_BM-2) resulted in a significant reduction in post-peak deflection and post-crack toughness, which indicates a decrease in strain hardening behaviour. Such a drastic change in the failure response could be attributed to several reasons, such as matrix densification,[67] interfacial stress concentration from rigid/agglomerates of biochar,[22] potential disruption of fiber-matrix bonding[61] or to reduced fiber dispersion. Such effects are typical of fiber cement composites and has been reported with the inclusion of fine fillers, like, nanosilica[67] and nano/micro-cellulosic additives,[1,2] and matrix modifiers such as fly ash. Fly ash, in particualr, alters fracture behavior by modifying the microstructure and interfacial properties[61] due to poor/heterogeneous dispersion of fine fillers/additives at extremely low or high loadings.[68] Therefore, the observed shift reflects a loss of ductility and toughness due to microstructural and interfacial interactions, rather than a direct transition of failure mode (brittle fracture).

Further analysis of the stress–strain curves indicates that there is less room for the fibers to flex under load, limiting the load transfer, and thereby compromising the ductility of the composite. Note that fibers are tightly embedded (mechanical interlocking) in between the cement–biochar matrix. So, as the biochar and cement contents are varied proportionally while keeping the NBSK fibers content constant, we believe that further optimization—particularly through adjusting fiber dosage (increasing the content of NBSK fibers) and by optimising biochar loadings—could improve the strain hardening behaviour of the composite. In this study fiber dosages were

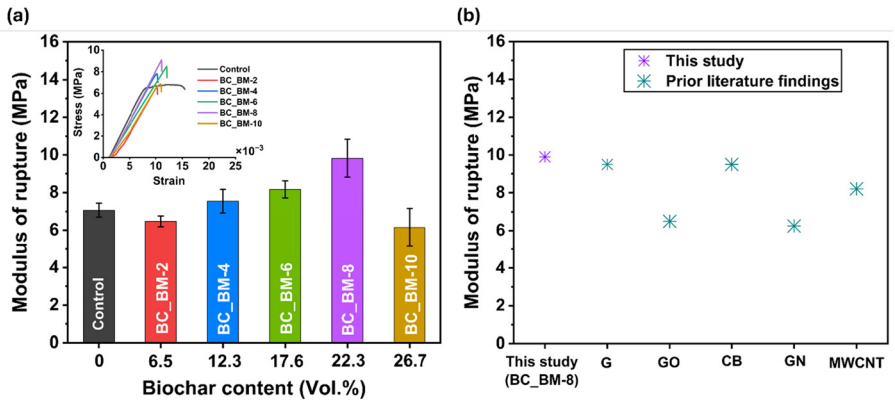

Fig. 5 Mechanical characterization and performance evaluation of fiber cement with biochar as a function of biochar content. (a) Stress–strain curves and the calculated modulus of rupture (MOR), (b) MOR comparison between biochar and traditional carbon materials as SCMs. In Fig. 4d, G, GO, CB, GN, and MWCNT stand for graphene, graphene oxide carbon black, graphene nanoparticles and multiwalled carbon nanotubes, respectively.[62–66] More details pertaining to the composition and the type of dispersant/superplasticizer employed for these materials are mentioned in the ESI in Table S9.† All tested composites were cured for 28 d under ambient conditions unless stated otherwise.

 This journal is © The Royal Society of Chemistry 2025

Open Access Article. Published on 04 July 2025. Downloaded on 4/7/2026 8:36:45 PM. This article is licensed under a Creative Commons Attribution-NonCommercial 3.0 Unported Licence.

intentionally kept constant at 8 wt%, following conventional loading practices adopted in FC research.[1] To this end, our prior work has shown that it is possible to counteract matrix densification and induce flexibility by carefully optimising fiber/additive loading in FC.[2] Although we have demonstrated this potential, further investigation with biochar is beyond the scope of this study.

Moreover, the particle size and morphology of biochar particles significantly influence the mechanical behaviour (*i.e.*, flexural response) and failure modes of fiber cement. Ball milling of biochar homogenized particle size and shape as shown in Fig. 1(a–h) and Fig. S2†, which possibly contributed to improvement in packing density and matrix densification. As a result, peak strength was increased upto 22.3 (vol%) of biochar addition. However, the same ball milling process may also compromise the ductility (Fig. 5(a)), as finer and more angular particles (see Fig. 1(a–h) and Fig. S2†) can interfere with fiber dispersion and reduce fiber matrix bonding. Thus, it can limit the effectiveness of the NBSK fiber in bridging cracks. So, the failure response of these materials observed a shift from ductile to a more matrix dominated brittle fracture. Note that these interactions can differ significantly from the mechanisms discussed in prior studies, which focused solely on matrix modifications, where the ductility seems to have been enhanced with the addition of biochar.[69]

Fig. 5a depicts the variation of MOR with the biochar content (0–10 wt%), which is the replacment of the OPC content in the matrix. Interestingly, at a low biochar content (*i.e.*, 4 wt%), MOR increased by 17% and the trend continued until 8 wt%, reaching a maximum of 9.8 MPa (40% increase). Interestingly, irrespective of the replacement of cement with biochar, the calculated MOR has been higher than the pristine cement matrix for all biochar concentrations (with an exception at 2 wt%) where the MOR was maintained with that of control. Because the incorporation of biochar can have an impact on the packing density[13] while its polar surface chemistry and porous morphology can host nucleation sites favouring the ongoing hydration reactions.[70] In addition to this, the presence of NBSK fibers and biochar can retain water, which is available during the mixing of FC slurry (affecting the overall W/B ratio of FC slurry) and release it over time as the FC cures. Such a phenomenon affords unhydrated cement to hydrate over time, facilitating a mechanism termed internal curing, resulting in strength development. All these are crucial parts of the strengthening mechanism, *i.e.*, an increase in peak strength as evidenced by the high MOR values. On the other hand, upon increasing the content of biochar to 10 wt%, the mean MOR reduced to 6.1 MPa from 9.8 MPa (54% reduction *vs.* BC_BM-8). Such a trend has been reported in prior research where excessive biochar in the matrix acts as a potential stress concentrator owing to the particle agglomeration,[16] especially when no surfactant or dispersing agents are added in the formulation. Another possible reason for such failures, especially at high biochar dosages could be attributed to the inherent porous nature of biochar that can lead to the formation of potential air voids in the tensile plane of the cement composites compromising structural integrity as reported by Khushnood *et al.*[18] Moreover, the evolution of '$\tau_{static}/\tau_{dynamic}$' trends observed in this study was in accordance with the MOR trends with increasing biochar content (*vide supra*) – indicating a direct correlation with these important rheo-mechanical properties (see Fig. S4(a and b)†).

Finally, from Fig. 5(b), MOR of FC with 8 wt% of biochar (BC_BM-8) is compared against traditional carbon materials, such as carbon black (CB),[64] graphene (G),[62] graphene oxide (GO),[63] graphene nanoparticles (GN)[65] and MWCNT.[66] As exhibited in Fig. 5(b), BC_BM-8 MOR is significantly higher (34%, 36% and 17%, respectively) than GO,[63] GN[65] and MWNT,[66] respectively. However, MOR values of cement composites with G[62] and CB[64] were comparable with BC_BM-8. A crucial point to note is that the reported carbon materials require dispersing agents/surfactants/superplasticiser and fine/coarse aggregates to improve particle distribution, which in turn contribute to flexural strength development (see Table S9† for more details).

Role of biochar in cement chemistry at the fiber–cement interface

Microstructural and hydration product characterization. The reaction of cement clinker phases with water results in the formation of hydrates (known as OPC hydration products), which impart strength to the cement composite.[71] Now with the addition of biochar as an SCM, it's essential to understand how biochar may influence the hydration product formation. Thus, PXRD (for phase ID) and solid-state NMR were employed to understand the structure and speciation of cement hydration products.

Fig. 6(b) depicts the PXRD patterns of reference OPC (unhydrated) and fiber cement (hydrated, 28-day cured) containing biochar (BC_BM-8). The composition (phase ID) of the cement clinker phases present in OPC is depicted in the PXRD curves represented in Fig. 6(a) and is adopted from our past study.[1] PXRD of (BC_BM-8) revealed distinct peaks at 2θ = 9° and 35° for ettringite and 2θ = 17° for portlandite, respectively, which were absent in the PXRD of OPC, confirming cement hydration.[1] Peaks at 2θ = 16°, 29°, 32°, and 49° were ascribe to the CSH, which is considered as the primary hydration product in cured fiber cement (BC_BM-8).[72] Peak overlaps between ettringite and portlandite at 2θ = 17° and between CSH and calcite peaks at 2θ = 29° were observed.[1] Additional crystalline phases beyond conventional OPC hydration products were not detected.

Visual evidence from SEM suggests the possibility of OPC hydration product (*e.g.*, CSH) formation, localised near biochar particles – both within the cement–biochar matrix Fig. 6(a and b) and within the vicinity of biochar particles (Fig. 6(c)). However, SEM analysis alone is inadequate to characterize the complex chemical composition of OPC hydration products. The semicrystalline CSH, is also challenging *via* conventional PXRD technique.[73] Additionally, the occurrence of overlapping peaks between CSH and other hydration products creates uncertainty in deciphering the

Open Access Article. Published on 04 July 2025. Downloaded on 4/7/2026 8:36:45 PM.
This article is licensed under a Creative Commons Attribution-NonCommercial 3.0 Unported Licence.

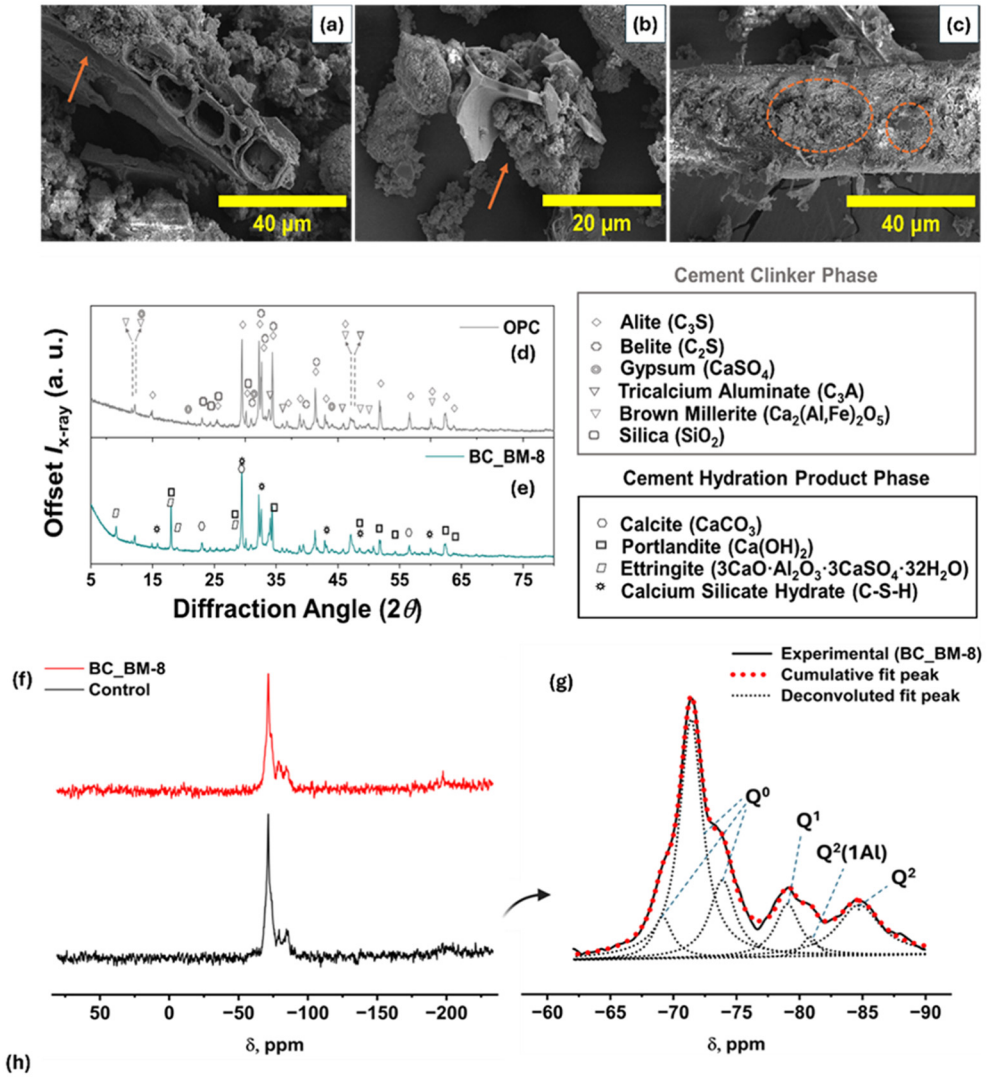

(h)

Sample	Content of silicate species (%)				Degree of hydration (%)
	Q^0	Q^1	$Q^2(1Al)$	Q^2	
Control	75.17	6.98	0.90	16.93	24.82
BC_BM_8	70.35	11.31	1.77	16.54	29.64

Fig. 6 Microstructural and hydration product characterization of fiber cement. (a–c) SEM micrographs of fiber cement (BC_BM-8). In (a–b), the orange arrows indicate the growth of OPC hydration products on the biochar surface, and in (c), the orage circle indicates the formation of possible hydration products at fiber-cement interface. (d–e) PXRD patterns of fiber cement (BC_BM-8) and OPC as reference. (f) Raw ^{29}Si MAS NMR spectrum of control and fiber cement (BC_BM-8). (g) Deconvoluted ^{29}Si MAS NMR spectrum of fiber cement (BC_BM-8). (h) Summary of spectral deconvolution results. Note, for NMR analysis, NBSK fibers were not employed to negate its effect on hydration products and 7 days curing was sufficient. The PXRD diffractogram of raw biochar is shown in Fig. S5† and the OPC reference diffractogram has been collected from our past study.[1] The powder diffraction file (PDF) numbers associated with the OPC clinker phases (anhydrous state) and hydrated state have been obtained from the ICDD database, which are as follows: Alite (00-055-0738), Belite (00-033-0302), Gypsum (01-074-1905), Tricalcium aluminate (01-074-7039), Brownmillerite (01074-3674), Silica (01-071-0261), calcite (01-086-2334), portlandite (00-001-1079), and Ettringite (01-0757554).[75]

appropriate peaks with confidence, making phase quantification difficult.[74] Therefore, the effect (if any) of biochar on the structural conformation of silicates in CSH deemed to be difficult *via* SEM and PXRD techniques. Note that further exploration with these techniques were not explored. Hence, in such a case, solid-state NMR could be useful.

^{29}Si MAS NMR has been widely used to study the silicate species (degree of hydration and polymerization) around CSH,

 This journal is © The Royal Society of Chemistry 2025

Open Access Article. Published on 04 July 2025. Downloaded on 4/7/2026 8:36:45 PM. This article is licensed under a Creative Commons Attribution-NonCommercial 3.0 Unported Licence.

which is the primary OPC hydration product, as discussed in the above sections.[76] The environment around silicate species (conformation of silicates) in ^{29}Si NMR is given by Q^n, where 'n' denotes the number of Si–O–Si linkages. Q^0 represents the isolated silicate species (silicon oxygen tetrahedra) belonging to the unhydrated cement clinker phases (C_2S, C_3S) and has a chemical shift observed in the range (−68 to −76 ppm).[77,78] It's important to note that Q^0 comprises multiple resonances caused due to the presence of alite and belite phases in OPC, with resonance due to C_3S, occurring at a higher chemical shift compared to C_2S.[78] This combined resonance results in the broadening of the Q^0 peaks, therefore multiple peaks (at δ = −69.1, −71.3, and −73.8 ppm) are assigned to deconvolute and quantify the Q^0 species (see Fig. 6(g)).

Now, as OPC undergoes hydration, Q^1 (−76 to −82 ppm) and Q^2 (−82 to −88 ppm) species are formed at the expense of Q^0 species.[79] Therefore, there are tentative peaks at δ = −79 assigned to Q^1, at δ = −80.8 ppm assigned to Q^2 (1Al) and a peak at δ = −84.7 ppm, assigned to Q^2 sites respectively.[80] Additionally, prior research from Anderson *et al.*, has confirmed the resonance of Q^2 (1Al) sites in coreesponding to the aluminate phase in C_3A and C_4AF. In such a case, one of the two bridging oxygen atoms is bonded to Al, and thereby replacing Si in the silicate tetrahedra.[81] Q^3 and Q^4 (higher polymerised silicate networks) are typically absent in OPC hydration product phases and their presence is often observed with the addition of silicate based admixtures in the cement.[82]

Fig. 5(f) depicts the raw ^{29}Si MAS NMR spectrum of 7 day cured control and fiber cement (BC_BM-8) sample, respectively. Fig. 6(g) describes the deconvoluted spectrum of the BC_BM-8 sample. From characteristic peaks occurring at chemical shifts (*vide supra*) are assigned to deconvolute and quantify the different silicate species. Fig. 6(h) summarises the results from the spectral deconvolution and by quantifying the amount of silicate species, degree of silicate hydration (α) is possible to quantitate using the formula α (%) = 100 − Q^0 (%).[83] It may be noted that cement curing and subsequent strength development, occur progressively at an interval of 7 days (for *e.g.*, 7, 14, 21, and 28 days). 7 day cured samples were used for NMR analysis, as hydration at this stage is advanced enough to identify distinct silicate species, without the complexity introduced by later stage silicate polymerisation.

From Fig. 6(h), a reduction in Q^0 species (*vs.* control) indicates possible increase in the degree of hydration. This means that isolated silicate species (Q^0 species) in clinker phases converted into polymerised silicate species (Q^1, Q^2) in presence of biochar in fiber cement (excluding the effects of NBSK fibers). Additionally, as shown in Fig. 5(h), amount of Q^1 species increased (64%) while amount of Q^2 species did not increase. This means that the incorporation of biochar possibly have altered the environment around silicate species, favouring the formation of fragmented polymerised silicate species (Q^1) compared to the formation of polymerised silicate networks (such as Q^2 species), especially during the early age curing (*i.e.*,7 days in this case). This in a way validates the visual evidence that biochar may have acted as nucleation points for additional precipitation of hydration products (referred to as secondary CSH in this case) to develop.

We ascribe this ability of biochar to its physicochemical characteristics, especially surface chemical functionality. The inference derived from the high resolution deconvoluted XPS spectrum of C and O – indicates the presence of surface functional groups (in relatively high proportions) that are capable of being reactive with the cement clinker phases in the high alkaline environment present in the cement matrix. Additionally, evidence from past studies has shown that the presence of hydroxyl and carboxyl linkages in the cement admixtures/additive can form active nucleation sites which could promote the precipitation of early CSH. This happens because the hydroxyl and carboxyl functional groups present in biochar can potentially interact with calcium ions in cement pore solution (wet state while mixing) – which prompts the calcium ions to localise near hydroxyl groups. Simultaneously, silicate ions (from dissolved clinker phases) are also drawn to the hydroxyl groups, thus facilitating a close interaction between calcium and silicate species. Overall, based on the SEM, PXRD and NMR, the key message we can infer is that presence of biochar possibly promotes the formation of poorly crystalline CSH.[84] This early precipitation of CSH then acts as anchoring points for this process to proceed further, and the corresponding binding of these CSH phases accumulates to form connected CSH networks (at the end of curing, typically after 28 days in an air cured system). Note that similar nucleation effects have been reported with other carbon based admixtures such as graphene/graphene oxide in cement systems.[85]

Role of biochar in CO_2 footprint and cost to performance of fiber cement: balance between performance, cost and sustainability

The environmental impact of replacing high CO_2 emitting Portland cement with biochar was evaluated using a cradle-to-gate life cycle impact assessment, and the resulting global warming potential, GWP (in kg CO_2eq), as an indication of GHG emissions. The results were compared against the control sample (100% cement) and with the reported GWP of commercial fiber cement. From Fig. 7(a), it's observed that with the substitution of biochar (2 to 10 wt%), the net GWP values decreased (from 0.577 to 0.4458 kg CO_2eq.), leading to a reduction up to 22.8% (*vs.* control) and 24% (*vs.* commercial FC) for 10 wt% supplementation of biochar. This reduction could be attributed to the reduced cement content in the sample due to biochar substitution (minor contributor), coupled with the enhanced carbon sequestration potential of the supplemented biochar (major contributor). Additionally, from the performance point of view, it was observed from the rheo-mechanical study that the sample with an 8 wt% addition of biochar exhibited the best rheo-mechanical properties (*vs.* control), which corresponds to an 18.1% reduction in the net GWP result (*vs.* control). Moreover, the presence of cellulosic fibers (as reinforcement) adds to the carbon sequestration potential of the developed fiber cement. Note that for simpli-

Open Access Article. Published on 04 July 2025. Downloaded on 4/7/2026 8:36:45 PM.
This article is licensed under a Creative Commons Attribution-NonCommercial 3.0 Unported Licence.

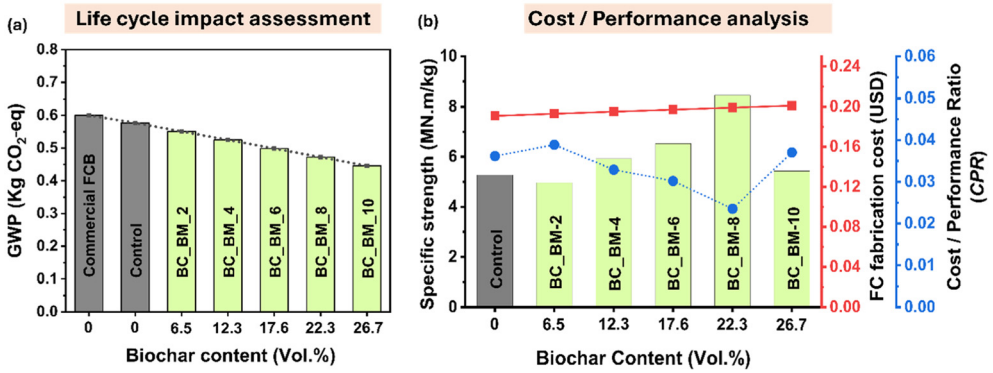

Fig. 7 Role of biochar in CO_2 footprint and cost to performance of fiber cement. (a) The accumulative GWP of different biochar supplemented FC, calculated using the EN 15804 A1:2020 assessment methodology, depicting the GWP impacts related to FC production (accounts for, raw material extraction, conversion and processing, and core process involved in the FC fabrication process and the benefit of supplementing different proportion of biochar as cement replacement). Note that the GWP results computed from this study were compared with those reported in a published LCA of a leading commercially available cellulose fiber reinforced FC board manufacturer (refer Table S12†) and with the control sample (BC_BM_0). Refer to the ESI (Fig. S6, and Tables S10, S11†) for further information regarding system boundary, functional unit and energy calculations. (b) Cost to performance analysis of FC with increasing biochar loading.

city of the analysis, the carbon sequestration potential of cellulosic fibers is not considered for this study as all the samples contain an equal proportion of fibers. Thus, the findings of LCA study demontrate a sustainable pathway for fiber cement fabrication with biochar as SCMs.

Understanding the cost/performance (C/P) characteristics of fiber cement is of utmost importance as we evaluate the practical implication of transitioning our lab scale product to the industrial scale. Considering this, a basic C/P analysis was conducted as shown in Fig. 7(b). The specific flexural strength of the fabricated FC was chosen as the performance metric of interest, compared against its associated cost of fabrication (in USD). This parameter was chosen considering the importance of lightweight composites for non-structural applications (used as facades). Additionally, a CPR index has been introduced as a measure of the effectiveness of C/P of FC samples. This way, it is possible to gain a quantitate perspective as to how the performance metrics and cost vary with the introduction of biochar in the FC system.

From the C/P analysis, it can be observed that the specific strength of fiber cement increased with biochar content (except at 10 wt% – specific strength was decreased, due to poor mechanical performance) indicating the potential of biochar in reducing the overall density of the composite. Note that commercial fiber cement is commonly characterized as a high-density facade panels, which is possiby further enahnced as biochar density ($\rho_{biochar}$ = 0.223 g cm^{-3}) is app. 15% less than conventional OPC (ρ_{cement} = 1.44 g cm^{-3}). Besides, physical characteristics such as high surface area and porosity of biochar also enables less amount of biochar particles to fill the fiber-cement interface. On the other hand, fabrication cost increased linearly with biochar substitution. For instance, with 8 wt% biochar substitution, occupying 22.3% by volume of FC, resulting in an increase in cost by 4.1%. Despite this increase in the FC fabrication cost, the CPR showed a decreasing trend (excluding 10 wt%) with the substitution of biochar, underscoring the opportunities with biochar to develop economically viable, low carbon, high performance building materials. Importantly, lighweight anf high strengt are critical parameters high rise buildings and offshore systems.

Conclusion

In this research, we have demonstrated a pathway to develop low carbon, lightweight, and high-strength fiber cement composite. The key findings from this study are as follows:

- The process of ball milling can alter the physicochemical properties of biochar (surface area, porosity, and degree of graphitization) and help attain good compatibility with the cement matrix, essential to produce low carbon-lightweight-high strength fiber cement composites.
- The results from the rheological characterization revealed that the static yield stress of the fiber-cement slurry increased with biochar content (reaching a maximum of 52.07 Pa at 10 wt% biochar content, exhibiting 98% increase *vs.* control), whereas the dynamic yield stress was independent of the biochar content. The increase in static yield stresss was alluded to the combined effect of (a) complex physiochemical interaction of FC constituents within the slurry causing resistance to flow (*i.e.*, the presence of clinker phases), NBSK fibers and biochar indulge in complex interactions (such as flocculation, van der Waals forces, electrostatic interactions, hydrogen bonding and physical entanglement within the FC slurry) and (b) structural build up, arising due to OPC hydration – leading to the formation of a primary and secondary CSH network (formed due to the ability of biochar to act as nucleation points). Additionally, the thixotropic behaviour of FC slurry improved with the biochar content. These properties are par-

 This journal is © The Royal Society of Chemistry 2025

Open Access Article. Published on 04 July 2025. Downloaded on 4/7/2026 8:36:45 PM. This article is licensed under a Creative Commons Attribution-NonCommercial 3.0 Unported Licence.

ticularly useful when it comes to mixing, pumping and consolidation steps during fabrication of fiber cement.

• Mechanical characterization revealed that the addition of biochar enhanced the flexural strength of the FC composite, with 8 wt% biochar replacement (accounting for 22.3 vol% of FC contributing to a 40% increase in flexural strength, *vs.* control). However, the stress–strain behaviour indicates that post-peak deflection and post-crack toughness were reduced.

• Microstructural, surface and bulk chemical analysis studies *via* SEM, XPS, Raman, PXRD, and ^{29}Si MAS NMR revealed that degree of hydration was possibly influenced by biochar in fiber cement. The benefits in cement hydration is important as biochar has high CO_2 removal potential. Based on spectroscopic analysis, the mechanism of strength development in biochar substituted fiber cement can be attributed to both physical and chemical properties of biochar, which promotes densification and can serve as potential nucleation sites for hydration products.

• Cradle to gate LCA analysis revealed that biochar can contribute to up to 18% for BC_BM-8 reduction in GWP emissions for BC_BM-8. Additionally, C/P analysis indicates that the incorporation of biochar increases the fabrication cost with a 4.2% increase for the BC_BM-8. However, rise in cost can be compensated by specific strength improvement as demonstrated by the CPR and a reduction in net CO_2 emission.

Author contributions

Conceptualization: S. R. & E. J. F., methodology: S. R. & M. H., investigation (experiments): S. R., A. J., A. G., and F. B. S., formal analysis: S. R. & M. H., visualisation: S. R., M. H., B. Z. & Q. T. writing – original draft: S. R., writing – editing: S. R., M. H., B. Z., A. G., E. J. F., & Q. T., and funding acquisition and supervision: E. J. F. All authors have read and approved the final manuscript.

Conflicts of interest

There are no conflicts of interest to declare.

Data availability

The data supporting this article have been included as part of the ESI.†

Acknowledgements

The authors gratefully acknowledge the financial support provided by the NSERC Canfor Industrial Research Chair in Advanced Bioproducts (# 553449-19), the NSERC Discovery Grant (RGPIN-2021-03172), the Canada Foundation for Innovation (Project number 022176) and the Pacific Economic Development Canada (PacifiCan). The authors also acknowledge technical and instrumental support from Anita Lam, Department of Chemistry, The university of British Columbia, Canada, Eric Ye, Department of Chemistry, Simon Fraser University, Canada, Gwenael Chamoulaud, Department of Chemistry, University of Quebec at Montreal, Canada and the Jeffrey D. Henderson, Surface Science Western, University of Western Ontario, Canada.

References

1 S. Raghunath, M. Hoque and E. J. Foster, *ACS Sustainable Chem. Eng.*, 2023, **11**, 10727–10736.
2 S. Raghunath, M. Hoque, B. Zakani, A. M. Gondaliya and E. J. Foster, *RSC Sustainability*, 2024, **2**, 3362–3374.
3 A. Herring, P. L. King, M. Saadatfar, F. Mahdini, A. M. K. Yahyah and E. Andò, *J. CO2 Util.*, 2021, **47**, 101494.
4 C. W. Hargis, I. A. Chen, M. Devenney, M. J. Fernandez, R. J. Gilliam and R. P. Thatcher, *Materials*, 2021, **14**, 2709.
5 C. F. Dunant, S. Joseph, R. Prajapati and J. M. Allwood, *Nature*, 2024, **629**(8014), 1055–1061.
6 Climate change: The massive CO2 emitter you may not know about, **https://www.bbc.com/news/science-environment-46455844**, (accessed 2 November 2024).
7 A. Sirico, P. Bernardi, C. Sciancalepore, F. Vecchi, A. Malcevschi, B. Belletti and D. Milanese, *Constr. Build. Mater.*, 2021, **303**, 124500.
8 J. Lehmann and S. Joseph, *Biochar for Environmental Management*, 2015, pp. 165–193.
9 J. A. Ippolito, L. Cui, C. Kammann, N. Wrage-Mönnig, J. M. Estavillo, T. Fuertes-Mendizabal, M. L. Cayuela, G. Sigua, J. Novak, K. Spokas and N. Borchard, *Biochar*, 2020, **2**, 421–438.
10 A. Tomczyk, Z. Sokołowska and P. Boguta, *Rev. Environ. Sci. Biotechnol.*, 2020, **19**, 191–215.
11 J. Lehmann, A. Cowie, C. A. Masiello, C. Kammann, D. Woolf, J. E. Amonette, M. L. Cayuela, M. Camps-Arbestain and T. Whitman, *Nat. Geosci.*, 2021, **14**(12), 883–892.
12 R. Roychand, S. Kilmartin-Lynch, M. Saberian, J. Li, G. Zhang and C. Q. Li, *J. Cleaner Prod.*, 2023, **419**, 138205.
13 A. Dixit, S. Gupta, S. D. Pang and H. W. Kua, *J. Cleaner Prod.*, 2019, **238**, 117876.
14 S. Gupta, J. M. Tulliani and H. W. Kua, *Sci. Total Environ.*, 2022, **807**, 150884.
15 W. C. Choi, H. Do Yun and J. Y. Lee, *J. Korea Inst. Struct. Maint. Insp.*, 2012, **16**, 67–74.
16 S. Gupta, H. W. Kua and S. D. Pang, *Constr. Build. Mater.*, 2018, **167**, 874–889.
17 L. Restuccia and G. A. Ferro, in Proceedings of the 9th International Conference on Fracture Mechanics of Concrete and Concrete Structures, IA-FraMCoS, 2016.
18 R. A. Khushnood, S. Ahmad, L. Restuccia, C. Spoto, P. Jagdale, J. M. Tulliani and G. A. Ferro, *Front. Struct. Civ. Eng.*, 2016, **10**, 209–213.

Open Access Article. Published on 04 July 2025. Downloaded on 4/7/2026 8:36:45 PM. This article is licensed under a Creative Commons Attribution-NonCommercial 3.0 Unported Licence.

19 A. Sirico, P. Bernardi, C. Sciancalepore, F. Vecchi, A. Malcevschi, B. Belletti and D. Milanese, *Constr. Build. Mater.*, 2021, **303**, 124500.
20 A. Chakraborty, M. Sain and M. Kortschot, *Holzforschung*, 2005, **59**, 102–107.
21 S. Kushwah, S. Singh, R. Agarwal, N. S. Nighot, R. Kumar, H. Athar and S. Naik B, *J. Mater. Sci.:Mater. Eng.*, 2024, **19**, 1–15.
22 S. Gupta, H. W. Kua and C. Y. Low, *Cem. Concr. Compos.*, 2018, **87**, 110–129.
23 Particle Size, **https://www.sympatec.com/en/particle-measurement/glossary/fundamentals-of-particle-characterisation/particle-size**, (accessed 12 December 2024).
24 QICPIC-RODOS-L-VIBRI-L, **https://www.sympatec.com/en/particle-measurement/sensors/dynamic-image-analysis/qicpic/qicpic-rodos-l-vibri-l**, (accessed 16 April 2025).
25 ASTM C1185, Standard Test Methods for Sampling and Testing Non-Asbestos Fiber-Cement Flat Sheet, Roofing and Siding Shingles, and Clapboards, West Conshohocken, 2016.
26 Z. P. Bazant and P. A. Pfeiffer, *Mater. J.*, 1987, **84**, 463–480.
27 Z. P. Bažant, *J. Eng. Mech.*, 1984, **110**, 518–535.
28 A. Carpinteri, B. Chiaia and P. Cornetti, *Materials for Buildings and Structures*, 2000, pp. 132–137.
29 R. Heu, S. Shahbazmohamadi, J. Yorston and P. Capeder, *Microsc. Today*, 2019, **27**, 32–36.
30 M. Finkbeiner, A. Inaba, R. B. H. Tan, K. Christiansen and H. J. Klüppel, *Int. J. Life Cycle Assess.*, 2006, **11**, 80–85.
31 P. Conte, R. Bertani, P. Sgarbossa, P. Bambina, H. P. Schmidt, R. Raga, G. Lo Papa, D. F. Chillura Martino and P. Lo Meo, *Agronomy*, 2021, **11**, 615.
32 S. C. Peterson, M. A. Jackson, S. Kim and D. E. Palmquist, *Powder Technol.*, 2012, **228**, 115–120.
33 G. James, D. A. Sabatini, C. T. Chiou, D. Rutherford, A. C. Scott and H. K. Karapanagioti, *Water Res.*, 2005, **39**, 549–558.
34 Y. Li, H. Lin, Y. Li, J. Shen, C. Yang and K. Wang, *ACS Sustainable Chem. Eng.*, 2024, **12**(37), 13826–13839.
35 Z. Wang, X. Pan, S. Kuang, C. Chen, X. Wang, J. Xu, X. Li, H. Li, Q. Zhuang, F. Zhang and X. Wang, *Int. J. Environ. Res. Public Health*, 2022, **19**, 7282.
36 Q. Fang, B. Chen, Y. Lin and Y. Guan, *Environ. Sci. Technol.*, 2014, **48**, 279–288.
37 J. Jung and A. H. Macdonald, *Phys. Rev. B:Condens. Matter Mater. Phys.*, 2013, **87**, 195450.
38 B. Arias, C. Pevida, J. Fermoso, M. G. Plaza, F. Rubiera and J. J. Pis, *Fuel Process. Technol.*, 2008, **89**, 169–175.
39 A. P. Terzyk, *Colloids Surf., A*, 2001, **177**, 23–45.
40 Y. Li, X. Zhang, R. Yang, G. Li and C. Hu, *RSC Adv.*, 2015, **5**, 32626–32636.
41 A. Ferrari and J. Robertson, *Phys. Rev. B:Condens. Matter Mater. Phys.*, 2000, **61**, 14095.
42 G. S. Dos Reis, S. H. Larsson, M. Thyrel, T. N. Pham, E. C. Lima, H. P. de Oliveira and G. L. Dotto, *Coatings*, 2021, **11**, 772.
43 M. González-Hourcade, G. Simões dos Reis, A. Grimm, V. M. Dinh, E. C. Lima, S. H. Larsson and F. G. Gentili, *J. Cleaner Prod.*, 2022, **348**, 131280.
44 N. J. Balmforth, I. A. Frigaard and G. Ovarlez, *Annu. Rev. Fluid Mech.*, 2014, **46**, 121–146.
45 P. Moller, A. Fall, V. Chikkadi, D. Derks and D. Bonn, *Philos. Trans. R. Soc., A*, 2009, **367**, 5139–5155.
46 M. Dinkgreve, J. Paredes, M. M. Denn and D. Bonn, *J. Non-Newton. Fluid Mech.*, 2016, **238**, 233–241.
47 P. C. F. Møller, J. Mewis and D. Bonn, *Soft Matter*, 2006, **2**, 274–283.
48 W. Mbasha, I. Masalova, R. Haldenwang and A. Malkin, *Appl. Rheol.*, 2015, **25**, 9–19.
49 C. Zhang, M. Wang, R. Liu, X. Li, Y. Liu, P. Jiang, J. Yan, Z. Zhu and M. Chen, *Constr. Build. Mater.*, 2023, **406**, 133498.
50 F. H. Marchesini, M. F. Naccache, A. Abdu, A. A. Alicke and P. R. de Souza Mendes, *Appl. Rheol.*, 2015, **25**, 32–41.
51 M. Cloitre and R. T. Bonnecaze, *Rheol. Acta*, 2017, **56**(3), 283–305.
52 S. Ma, Y. Qian and S. Kawashima, *Cem. Concr. Res.*, 2018, **108**, 1–9.
53 J. Zhang, Y. Su, C. Zhang, M. Li, X. Zhu, Y. Zhang and D. C. W. Tsang, *Constr. Build. Mater.*, 2024, **439**, 137358.
54 T. Wikström and A. Rasmuson, *Nord. Pulp Pap. Res. J.*, 1998, **13**, 243–250.
55 R. J. Kerekes, R. M. Soszynski and P. A. Tam Doo, in *Trans. of the VIIIth Fund. Res. Symp. Oxford, 1985*, ed. V. Punton, Fundamental Research Committee (FRC), Manchester, 1985, pp. 265–310.
56 T. Börzsönyi, B. Szabó, S. Wegner, K. Harth, J. Török, E. Somfai, T. Bien and R. Stannarius, *Phys. Rev. E:Stat., Nonlinear, Soft Matter Phys.*, 2012, **86**, 051304.
57 B. Zakani and D. Grecov, *Cellulose*, 2020, **27**, 9337–9353.
58 N. Roussel, G. Ovarlez, S. Garrault and C. Brumaud, *Cem. Concr. Res.*, 2012, **42**, 148–157.
59 H. Ye, J. Zhang, X. Gao, J. Ling, X. Zhu and D. Jiao, *Constr. Build. Mater.*, 2024, **411**, 134624.
60 S. Gupta, H. W. Kua and C. Y. Low, *Cem. Concr. Compos.*, 2018, **87**, 110–129.
61 K. Tosun-Felekoglu and B. Felekoglu, *Composites, Part B*, 2013, **52**, 62–71.
62 J. Liu, J. Fu, Y. Yang and C. Gu, *Constr. Build. Mater.*, 2019, **199**, 1–11.
63 Z. Pan, L. He, L. Qiu, A. H. Korayem, G. Li, J. W. Zhu, F. Collins, D. Li, W. H. Duan and M. C. Wang, *Cem. Concr. Compos.*, 2015, **58**, 140–147.
64 Q. Zhang, C. Luan, C. Yu, Y. Huang and Z. Zhou, *Constr. Build. Mater.*, 2022, **346**, 128455.
65 H. Sixuan, Master's Theses, Multifunctional Graphite Nanoplatelets (GNP) Reinforced Cementitious Composites, University of Singapore, 2012.
66 E. Cerro-Prada, R. Pacheco-Torres and F. Varela, *Materials*, 2021, **14**, 1–13.
67 H. Du, *Constr. Build. Mater.*, 2019, **199**, 696–704.
68 Y. Lin and H. Du, *Constr. Build. Mater.*, 2020, **265**, 120312.

 This journal is © The Royal Society of Chemistry 2025

Open Access Article. Published on 04 July 2025. Downloaded on 4/7/2026 8:36:45 PM.
This article is licensed under a Creative Commons Attribution-NonCommercial 3.0 Unported Licence.

69 M. Li, X. Zhu, Y. Zhang and D. C. W. Tsang, *Comput.-Aided Civ. Infrastruct. Eng.*, 2024, **39**, 3552–3572.
70 S. Gupta, P. Krishnan, A. Kashani and H. W. Kua, *Constr. Build. Mater.*, 2020, **262**, 120688.
71 H. F. W. Taylor, P. Barret, P. W. Brown, D. D. Double, G. Frohnsdorff, V. Johansen, D. Ménétrier-Sorrentino, I. Odler, L. J. Parrott, J. M. Pommersheim, M. Regourd and J. F. Young, *Mater. Constr.*, 1984, **17**, 457–468.
72 R. Maddalena, K. Li, P. A. Chater, S. Michalik and A. Hamilton, *Constr. Build. Mater.*, 2019, **223**, 554–565.
73 I. C. Madsen, N. V. Y. Scarlett and A. Kern, *Z. Kristallogr.*, 2011, **226**, 944–955.
74 R. Snellings, A. Salze and K. L. Scrivener, *Cem. Concr. Res.*, 2014, **64**, 89–98.
75 The International Centre for Diffraction Data, **https://www.icdd.com/**, (accessed 20 April 2025).
76 J. F. Young, *J. Am. Ceram. Soc.*, 1988, **71**, C118.
77 J. Hjorth, J. Skibsted and H. J. Jakobsen, *Cem. Concr. Res.*, 1988, **18**, 789–798.
78 Y. Dong, C. Feng, Q. Zhao and X. Liang, *Appl. Magn. Reson.*, 2019, **50**, 1345–1357.
79 A. S. Brykov, A. S. Vasil'Ev and M. V. Mokeev, *Russ. J. Appl. Chem.*, 2012, **85**, 1793–1799.
80 G. Parry-Jones, A. J. Al-Tayyib, S. U. Al-Dulaijan and A. I. Al-Mana, *Cem. Concr. Res.*, 1989, **19**, 228–234.
81 M. D. Andersen, H. J. Jakobsen and J. Skibsted, *Inorg. Chem.*, 2003, **42**, 2280–2287.
82 K. O. Kjellsen, *Cem. Concr. Res.*, 2000, **30**, 1323.
83 G. Le Saout, E. Lécolier, A. Rivereau and H. Zanni, *Cem. Concr. Res.*, 2006, **36**, 71–78.
84 C. Y. Huang, Y. C. Lin, J. H. Y. Chung, H. Y. Chiu, N. L. Yeh, S. J. Chang, C. H. Chan, C. C. Shih and G. Y. Chen, *Int. J. Mol. Sci.*, 2023, **24**, 10461.
85 S. Meng, X. Ouyang, J. Fu, Y. Niu and Y. Ma, *Nanotechnol. Rev.*, 2021, **10**, 768–778.